Preprints of the 22nd IFAC World Congress
Yokohama, Japan, July 9-14, 2023

Robust Nonlinear Self-Triggered Control Policy for a Novel Fully Actuated UAVs ⋆

Zhangzhen Zhu * **Yongliang Lin** * **Yu Zhang** *,** †

* *State Key Laboratory of Industrial Control Technology, College of Control Science and Engineering, Zhejiang University, Hangzhou, China*
** *Key Laboratory of Collaborative Sensing and Autonomous Unmanned Systems of Zhejiang Province, Hangzhou, China*

(e-mail: zhangzhenzhu@zju.edu.cn, zhangyu80@zju.edu.cn)

Abstract: This paper proposes a self-triggered control policy for a general kind of nonlinear system, ensuring robust performance under various perturbations and alleviating communication burden simultaneously. A novel fully actuated multirotors applied this method shows great robustness to perturbations and is able of tracking six dimensional decoupled trajectories without continuous background sensor monitoring. Rigorous input-to-state stability analysis is deduced and numerical simulations confirm the validity of the policy.

Keywords: UAVs, fully actuated, event-triggered, robustness, nonlinear systems

1. INTRODUCTION

In the last decades, multi-rotor UAVs have been widely used in aerial photography, logistics distribution and motion planning researches (Mellinger and Kumar (2011)). Simple reliable structure and succinct control algorithm are the main reasons for their large-scale deployments. Nevertheless, due to the intrinsic coupled translational and rotational dynamics, there are still many special applications beyond the competence of the traditional multi-rotor UAVs, like performing as stable aerial physical interaction platforms (see Staub et al. (2018); Suarez et al. (2018) and references therein) and operating in narrow environments. Therefore, a massive number of application scenarios require these fully actuated multirotors (FAM).

These novel FAM usually possess large flight envelopes which introduces complex nonlinearities. Therefore, many nonlinear control strategies have been proposed to improve the flighting performance, e.g., geometric control on SE(3) (Kaufman et al. (2014)), backstepping method (Li et al. (2017)) and feedback linearization method (Chang and Eun (2017)). The geometric controller (Lee et al. (2010)) utilizes the geometric property on nonlinear manifold to avoid the singularities of Euler angles and achieves almost globally exponentially convergence with tracking errors. Furthermore, a global chartwise feedback linearization method (Chang and Eun (2017)) for nonlinear dynamics was proposed for global tracking missions. However, these proposed control methods have few considerations on time varying perturbations which may cause instabilities during maneuvering flights or phisical interactions.

Moreover, these digital UAV systems typically contain multiple control loops that share limited computing resources. Therefore, the efficient use of these resources is of vitally importance. Classical digital control strategies update periodically and generate control sequences even unnecessary which leads to waste of communication resources. In order to solve this problem, scholars have proposed event triggering scheme in recent years (Tabuada (2007); Tallapragada and Chopra (2013); Abdelrahim et al. (2016)). To fulfill more flexible design requirements, dynamic event triggered policy has been introduced by Liu and Jiang (2019) and input-to-state stability of the controlled system is achievied. Moreover, to make this event triggered policy meaningful, infinite triggered counts should be avoided which is also called Zeno phenomenon (see Li et al. (2020)). However, both these schemes require a continuous background sensor supervision. Hence, to deal with this issue, a self-triggered control policy was introduced by Wang and Lemmon (2008), which also has $\mathcal{L}_2$ stability guarantee for linear systems.

Motivated by the aforementioned discussions, we aim to address the robust control problem of nonlinear systems under various perturbations and apply the derived methods to a novel FAM. Meanwhile, to cope with the limited communication source problem during various working conditions, background continuous sensor monitoring is not expected and a self-triggered control policy is needed. The main contribution of our work in this paper can be summarized as the following aspects.

1) We design a novel FAM which is capable of independently tracking arbitrary six dimensional trajectories and possesses ability of decoupled force and torque outputs.
2) A robust feedback linearization controller is designed

⋆ This work was supported by NSFC 62088101 Autonomous Intelligent Unmanned Systems, the National Key Research and Development Program of China under Grant 2021ZD0201403, the Project of State Key Laboratory of Industrial Control Technology, Zhejiang University, China (No.ICT2021A10), the Open Research Project of the State Key Laboratory of Industrial Control Technology, Zhejiang University ,China (No.ICT2022B04). († corresponding author).

so that the translational and rotational motion under the model uncertainties and external disturbances can be stabilized simultaneously. Meanwhile, precise model information is not needed any more.
3) A robust self-triggered control policy (without need of continuous background sensor monitoring) is first proposed for these linearizable MIMO nonlinear systems and input-to-state stability is guaranteed even under severe perturbations.

The rest of this article is organized as follows. Section 2 introduces some basic mathematical preliminaries and notations. Nonlinear rigid body dynamics and actuation properties are analyzed in Section 3. Section 4 introduces a robust feedback linearization method and a thorough nonlinear model for the novel UAVs is derived. Then self-triggered control policy is discussed and rigorous stability is proved in section 5. Finally, simulation results are illustrated to verify the validity of proposed controllers in section 6, before final conclusions in section 7.

2. PRELIMINARIES AND NOTATIONS

In this section, some mathematical preliminaries are summarized for understanding the contents in later sections. We start by introducing some families of functions.
A continuous function $\beta_1 : [0, a) \to [0, \infty)$, for some positive a, is said to belong to class $\mathcal{K}$ if it's strictly increasing and $\beta_1(0) = 0$. A continuous function $\beta_2 : [0, b) \times [0, \infty) \to [0, \infty)$ for some positive b belongs to class $\mathcal{KL}$, if for each fixed x, mapping $\beta_2(r, x)$ belongs to class $\mathcal{K}$ with respect to r and mapping $\beta_2(r, x)$ is decreasing with respect to x for each fixed r, meanwhile $\beta_2(r, x) \to 0$ as $x \to \infty$.
Next a quaternion belonging to 4D hypersphere embedded in $\mathbb{R}^4$ is defined as $\mathbf{q} := [\eta; \boldsymbol{\epsilon}]$, where $\eta \in \mathbb{R}$, and the vector part $\boldsymbol{\epsilon} \in \mathbb{R}^3$, and it's said to be unit quaternion if $\eta^2 + \|\boldsymbol{\epsilon}\|^2 = 1$. Multiplication of two quaternions $\mathbf{q}_1, \mathbf{q}_2$ is denoted as $\otimes$ in the following form (see Chapter 6 in Barfoot (2017)).

$$\mathbf{q}_1 \otimes \mathbf{q}_2 = \mathbf{Q}_1(\mathbf{q}_1)\,\mathbf{q}_2 = \mathbf{Q}_2(\mathbf{q}_2)\,\mathbf{q}_1$$
$$\mathbf{Q}_1(\mathbf{q}) = \begin{bmatrix} \eta & -\boldsymbol{\epsilon}^\top \\ \boldsymbol{\epsilon} & \eta\mathbf{I}_3 + [\boldsymbol{\epsilon}]_\times \end{bmatrix}, \mathbf{Q}_2(\mathbf{q}) = \begin{bmatrix} \eta & -\boldsymbol{\epsilon}^\top \\ \boldsymbol{\epsilon} & \eta\mathbf{I}_3 - [\boldsymbol{\epsilon}]_\times \end{bmatrix} \quad (1)$$

where $[\boldsymbol{\epsilon}]_\times$ is a skew symmetric matrix associated to the the vector part $\boldsymbol{\epsilon}$ (see (6.2) in Barfoot (2017)). Denote $\boldsymbol{\Omega}$ as the rigid body's angular velocity in body coordinate and the time derivative of the unit quaternion $\mathbf{q}$ can be written as (see Mayhew et al. (2011))

$$\dot{\mathbf{q}} = \frac{1}{2}\mathbf{Q}_2(\mathbf{q}) \begin{bmatrix} 0 \\ \boldsymbol{\Omega} \end{bmatrix} = \frac{1}{2} \begin{bmatrix} -\boldsymbol{\epsilon}^\top \\ \eta\mathbf{I}_3 - [\boldsymbol{\epsilon}]_\times \end{bmatrix} \times \boldsymbol{\Omega} \quad (2)$$

The Kronecker product for matrix $\boldsymbol{A} = (a_{ij})_{m\times n}, \boldsymbol{B} = (b_{ij})_{p\times q}$, is defined as below and its derived property for $\boldsymbol{C} = (c_{ij})_{n\times s}, \boldsymbol{D} = (d_{ij})_{q\times t}$ is also listed (see Graham (1981)).

$$\boldsymbol{A} \otimes \boldsymbol{B} = \begin{bmatrix} a_{11}\boldsymbol{B} & a_{12}\boldsymbol{B} & \dots & a_{1n}\boldsymbol{B} \\ a_{21}\boldsymbol{B} & a_{22}\boldsymbol{B} & \dots & a_{2n}\boldsymbol{B} \\ \dots & \dots & \dots & \dots \\ a_{m1}\boldsymbol{B} & a_{m2}\boldsymbol{B} & \dots & a_{mn}\boldsymbol{B} \end{bmatrix} \quad (3)$$

$$(\boldsymbol{A} \otimes \boldsymbol{B})(\boldsymbol{C} \otimes \boldsymbol{D}) = (\boldsymbol{AC}) \otimes (\boldsymbol{BD}) \quad (4)$$

Furthermore, some notation conventions used in the following paragraphs are listed here for clarity. We use ISS to represent input-to-state stability which was introduced in Sontag (1989). Besides, given a square matrix $\boldsymbol{P}$, we use $\lambda_m(\boldsymbol{P})$ and $\lambda_M(\boldsymbol{P})$ to represent the minimum and maximum eigenvalues of matrix $\boldsymbol{P}$ respectively.

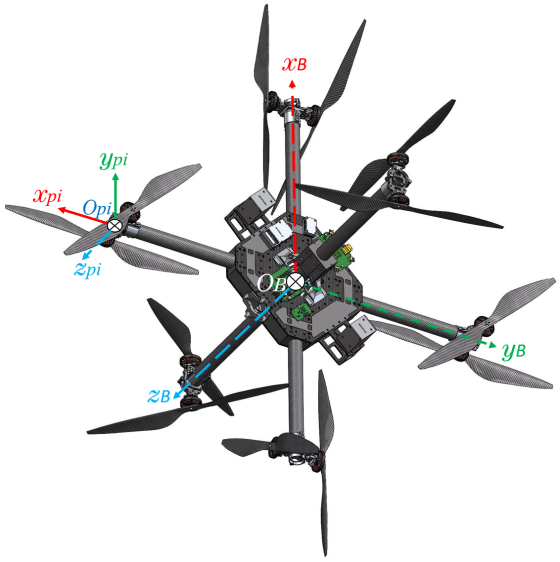

Fig. 1. Fully-actuated multirotor schematic.

3. DYNAMIC MODELS FOR FULLY-ACTUATED UAVS

In this section we consider the dynamic model of FAM which is capable of tracking decoupled trajectories. Three coordinate systems are introduced before discussing the detailed 6D motion. The North-East-Down (NED) inertial frame $\mathscr{F}_W = \{(\mathbf{x}_W, \mathbf{y}_W, \mathbf{z}_W), O_W\}$ attached to the earth. The body fixed frame $\mathscr{F}_B = \{(\mathbf{x}_B, \mathbf{y}_B, \mathbf{z}_B), O_B\}$ attached to the object, and the actuator frame $\mathscr{F}_{Pi} = \{(\mathbf{x}_{Pi}, \mathbf{y}_{Pi}, \mathbf{z}_{Pi}), O_{Pi}\}$ where $\mathbf{z}_{Pi}$ is collinear with the aeroforce. The FAM is modelled as a rigid body, and the body frame coincides with the principal axes of inertia at origin O_B. Coordinates of the FAM are illustrated in Fig. 1 including the body and actuator frame $\mathscr{F}_B$, $\mathscr{F}_{Pi}$.

3.1 Rigid Body Dynamics

Generally the flight envelope of the FAM is much larger than traditional UAVs and the corresponding aerodynamic forces together with propellers' operating conditions are more complicated. Hence, the FAM dynamic is derived considering both Newton-Euler approach (Siciliano and Khatib (2016)) and aerodynamic influences under several basic assumptions (Kai et al. (2017)) including hingeless propellers, windless environment, etc. Denote $\boldsymbol{R}(\tilde{\boldsymbol{q}}_{B/W}) = [\boldsymbol{\zeta_1}\ \boldsymbol{\zeta_2}\ \boldsymbol{\zeta_3}] \in \mathrm{SO}(3)$ as the rotation matrix describing the orientation of $\mathscr{F}_B$ with respect to $\mathscr{F}_W$, where $\tilde{\boldsymbol{q}} = \tilde{\boldsymbol{q}}_{B/W} = [q_0\ \boldsymbol{q}\ ] = [q_0\ q_1\ q_2\ q_3]^T$ is the corresponding quaternion. Meanwhile, $\boldsymbol{p} = \boldsymbol{p}_{B/W} \in \mathbb{R}^3$ denotes the position of O_B w.r.t. $\mathscr{F}_W$, and the velocity of the FAM measured in inertia frame $\mathscr{F}_W$ is denoted as $\boldsymbol{v}$.

$$\dot{\boldsymbol{p}} = \boldsymbol{v} \tag{5}$$

$$m\dot{\boldsymbol{v}} = \boldsymbol{R}(\tilde{\boldsymbol{q}})\boldsymbol{F_B} + m\boldsymbol{g} - \boldsymbol{R}(\tilde{\boldsymbol{q}})\boldsymbol{D}_{\mathrm{f}}\boldsymbol{R}(\tilde{\boldsymbol{q}})^{\top}\boldsymbol{v} \tag{6}$$

$$\dot{\boldsymbol{R}}(\tilde{\boldsymbol{q}}) = \boldsymbol{R}(\tilde{\boldsymbol{q}})\hat{\boldsymbol{\Omega}} \tag{7}$$

$$\boldsymbol{I}_{\mathrm{t}}\dot{\boldsymbol{\Omega}} = \boldsymbol{\tau_B} - \boldsymbol{\Omega} \times \boldsymbol{I}_{\mathrm{t}}\boldsymbol{\Omega} - \boldsymbol{\tau}_{\mathrm{g}} - \boldsymbol{C}\boldsymbol{R}(\tilde{\boldsymbol{q}})^{\top}\boldsymbol{v} - \boldsymbol{D}_{\mathrm{r}}\boldsymbol{\Omega} \tag{8}$$

where $\boldsymbol{\Omega} = (\Omega_x, \Omega_y, \Omega_z)$ denotes the FAM's angular velocity and $\boldsymbol{I}_{\mathrm{t}} \in \mathbb{R}^{3\times3}$ is the inertia tensor, both expressed in the body-fixed frame $\mathscr{F}_B$, $\boldsymbol{D}_{\mathrm{f}} = \mathrm{diag}\,(d_x, d_y, d_z)$ is a constant diagonal matrix which represents the flapping drag force coefficient, $\mathbf{C}$ and $\boldsymbol{D}_{\mathrm{r}}$ are constant matrices induced by aerodynamic configurations, $[\boldsymbol{F_B}\ \boldsymbol{\tau_B}] \in \mathbb{R}^6$ is the wrench input, and $\boldsymbol{\tau}_{\mathrm{g}} \in \mathbb{R}^3$ are gyroscopic torques induced by propellers. Detailed derivation process can be viewed in Kai et al. (2017). Performance of the FAM during maneuvering trajectories while neglecting these aerodynamics would cause poor performances.

3.2 Actuation Property Analysis

Wrenches (Siciliano and Khatib (2016)) mentioned in the previous section are generated by spinning motion of propellers in frame $\mathscr{F}_{Pi}$ as

$$f_i = \mathrm{sign}\,(\omega_i)\,C_f{\omega_i}^2 = \mathrm{sign}\,(\omega_i)\,C_f u_i \tag{9}$$

$$\tau_i = \mathrm{sign}\,(\omega_i)\,C_\tau{\omega_i}^2 = \mathrm{sign}\,(\omega_i)\,C_\tau u_i \tag{10}$$

where C_f and C_τ are aerodynamic constants, ω_i is rotation speed of the propeller, u_i is the virtual control input and $\mathrm{sign}\,(\omega_i)$ is valid when bidirectional actuator exists. Without loss of generality, three angle parameters $[\alpha\ \beta\ \gamma]$ are utilized to describe the wrench in $\mathscr{F}_B$ as illustrated in Fig. 2. Denote $\boldsymbol{R}_{B/P}(\alpha,\beta,\gamma)^T$ as the transfom matrix of wrench from $\mathscr{F}_{Pi}$ to $\mathscr{F}_B$, for notational convenience, let s and c represent sin and cos respectively.

$$\begin{aligned}\boldsymbol{R}_{B/P}(\alpha,\beta,\gamma) &= \tilde{\boldsymbol{\Gamma}}^T \\ &= \begin{bmatrix} c_\beta c_\gamma & c_\beta s_\gamma & -s_\beta \\ s_\alpha s_\beta c_\gamma - c_\alpha s_\gamma & s_\alpha s_\beta s_\gamma + c_\alpha c_\gamma & c_\beta s_\alpha \\ c_\alpha s_\beta c_\gamma + s_\alpha s_\gamma & c_\phi s_\beta s_\gamma - s_\alpha c_\gamma & c_\beta c_\alpha \end{bmatrix}\end{aligned} \tag{11}$$

The specific wrench expressed in $\mathscr{F}_B$ is derived as follow, where $\boldsymbol{l}_i$ is the actuator arm vector in $\mathscr{F}_B$, $\boldsymbol{\mathcal{W}}_f$ and $\boldsymbol{\mathcal{W}}_\tau \in \mathbb{R}^{3\times N}$ are the mapping matrix from the N actuators' input to the final wrench expressed in frame $\mathscr{F}_B$. Hence, $\boldsymbol{F_B}$, $\boldsymbol{\tau_B}$ that appear in (6) and (8) are defined as

$$\begin{aligned}\boldsymbol{\mathcal{W}}_{fi} &= \mathrm{sign}\,(\omega_i)\,C_f\tilde{\boldsymbol{\Gamma}}_i\mathbf{z}_{Pi} \\ \boldsymbol{\mathcal{W}}_{\tau i} &= \mathrm{sign}\,(\omega_i)\,C_\tau\tilde{\boldsymbol{\Gamma}}_i\mathbf{z}_{Pi} + \boldsymbol{l}_i \times \boldsymbol{\mathcal{W}}_{fi} \\ [\boldsymbol{F_B}\ \boldsymbol{\tau_B}] &= \begin{bmatrix} \sum_{n=1}^{N}\boldsymbol{\mathcal{W}}_{fi}u_i & \sum_{n=1}^{N}\boldsymbol{\mathcal{W}}_{\tau i}u_i \end{bmatrix} = \boldsymbol{\mathcal{W}}\boldsymbol{u}\end{aligned} \tag{12}$$

According to the wrench decoupling thesis in Michieletto et al. (2017), the control input $\boldsymbol{u} = \begin{bmatrix}\omega_1^2 & \cdots & \omega_N^2\end{bmatrix} \in \mathbb{R}^N$ can be split into two orthogonal subspaces $\mathrm{Im}\left(\boldsymbol{\mathcal{W}}_\tau^{\top}\right)$ and $\ker(\boldsymbol{\mathcal{W}}_\tau)$. A common and basic assumption is that the designed FAM is almost able to span whole torque space $\mathbb{R}^3$, i.e., $rank(\boldsymbol{\mathcal{W}}_\tau) = 3$. As we will see it clearly in (20), matrix $\mathcal{B}(\mathbf{x},\mathbf{t})$ has an rank of 6 almost everywhere thus the force output is completely decoupled with torques.

4. ROBUST FEEDBACK LINEARIZATION CONTROLLER

In this section three themes are analyzed the about feedback linearization (FBL) method which is an invaluable tool for solving nonlinear systems. First, the FBL approach to deal with the multi-input multi-outputs (MIMO) systems is introduced, and partially linearization is also discussed where an unobservable internal dynamics exists. Meanwhile the incremental form of the FBL and its robustness under perturbations is analyzed. Finally a thorough mathematical model of the designed FAM is illustrated.

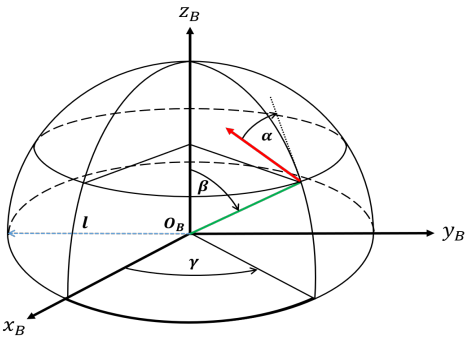

Fig. 2. Generic vector force described by $\alpha\ \beta\ \gamma$.

4.1 Feedback Linearization for MIMO Object

Consider an input-affine MIMO nonlinear system as:

$$\dot{\boldsymbol{x}} = \boldsymbol{f}(\boldsymbol{x}) + \boldsymbol{g}(\boldsymbol{x})\boldsymbol{u} = \boldsymbol{f}(\boldsymbol{x}) + \sum_{i=1}^{m} g_i(\boldsymbol{x})u_i \tag{13}$$

$$\boldsymbol{y} = \boldsymbol{h}(\boldsymbol{x}) = \mathrm{col}\,(y_1, \ldots, y_m) \tag{14}$$

where $\boldsymbol{x} \in \mathbb{R}^n$ is the state variable, $\boldsymbol{f} : \mathbb{R}^n \to \mathbb{R}^n$, $\boldsymbol{h} : \mathbb{R}^n \to \mathbb{R}^k$ are sufficient smooth and locally Lipschitz continuous in domain $D \subset R^n$ and $\boldsymbol{g}$ is the smooth input transform matrix: $\mathbb{R}^n \to \mathbb{R}^{n\times m}$. In this paper we only focus on the case where $k = m$.

Feedback linearizablity of a SISO system has been proved by theorems in Khalil (2014), and for nonlinear MIMO systems the essential proof idea of full-state feedback linearizablity is just the same.

An input-affine MIMO nonlinear system in form (13) is called to have a vectorized relative degree $\boldsymbol{r} = \{r_1, \ldots, r_m\}$ in $D_0 \subset D$ if matrix $\mathcal{B}(\boldsymbol{x})$ (see (15)) is nonsingular for all x in a neighborhood of D and for $\forall\ 1 \le j \le m$, $1 \le i \le m$, $L_{g_j}L_f^{r_i-1}h_i(\boldsymbol{x}) \neq 0$ in D_0. The Lie derivative is defined as $\mathcal{L}_f h_i = \frac{\partial h_i}{\partial \boldsymbol{x}}\boldsymbol{f}$ and $\mathcal{L}_{g_j}h_i = \frac{\partial h_i}{\partial \boldsymbol{x}}\boldsymbol{g}_j$.

$$\mathcal{B}(\boldsymbol{x}) = \begin{bmatrix} \mathcal{L}_{g_1}\mathcal{L}_f^{r_1-1}h_1(\boldsymbol{x}) & \cdots & \mathcal{L}_{g_m}\mathcal{L}_f^{r_1-1}h_1(\boldsymbol{x}) \\ \mathcal{L}_{g_1}\mathcal{L}_f^{r_2-1}h_2(\boldsymbol{x}) & \cdots & \mathcal{L}_{g_m}\mathcal{L}_f^{r_2-1}h_2(\boldsymbol{x}) \\ \vdots & \vdots & \vdots \\ \mathcal{L}_{g_1}\mathcal{L}_f^{r_m-1}h_m(\boldsymbol{x}) & \cdots & \mathcal{L}_{g_m}\mathcal{L}_f^{r_m-1}h_m(\boldsymbol{x}) \end{bmatrix} \tag{15}$$

Besides, $\mathcal{A}(\boldsymbol{x})$ is defined as:

$$\mathcal{A}(\boldsymbol{x}) = \begin{bmatrix}\mathcal{L}_f^{r_1}h_1(\boldsymbol{x}), \cdots, \mathcal{L}_f^{r_m}h_m(\boldsymbol{x})\end{bmatrix}^T$$

Now we denote the virtual control $\boldsymbol{\nu} = \mathcal{A}(\boldsymbol{x}) + \mathcal{B}(\boldsymbol{x})\boldsymbol{u}$ and $\boldsymbol{\nu}$ can be designed by various linear methods such as classic PD controller (details please see next subsection).

4.2 Robustness Analysis with Incremental Method

As mentioned in previous subsection, the controller $\boldsymbol{\nu}$ relies on precise model information thus the nonlinear

terms $\mathcal{A}(\boldsymbol{x})$ and $\mathcal{B}(\boldsymbol{x})$ can be completely compensated. However in actual environments, various uncertainties make this method impossible. To cope with this drawback, an incremental control form was proposed (Huang et al. (2017)) and so on. Here we take a brief introduction to it. Denote the system sampling interval as ΔT_s, the previous sampling state as $\boldsymbol{x}_0 = \boldsymbol{x}(t-\Delta T_s)$ and the previous virtual control $\boldsymbol{\nu}_0$ equals $\boldsymbol{\nu}(t-\Delta T_s)$, then according to the analysis in last subsection, we can obtain that

$$\begin{aligned}\boldsymbol{y}^{(\boldsymbol{r})} &= \boldsymbol{\nu} = \mathcal{A}(\boldsymbol{x}) + \mathcal{B}(\boldsymbol{x})\boldsymbol{u} \\ &= \boldsymbol{\nu}_0 + \left.\frac{\partial \boldsymbol{y}^{(\boldsymbol{r})}}{\partial \boldsymbol{x}}\right|_{\boldsymbol{x}_0} \Delta\boldsymbol{x} + \mathcal{B}\left(\boldsymbol{x}_0\right)\Delta\boldsymbol{u} + O\left(\Delta\|\boldsymbol{x}\|^2\right) \\ &= \boldsymbol{\nu}_0 + \mathcal{B}\left(\boldsymbol{x}_0\right)\Delta\boldsymbol{u} + \delta(\boldsymbol{\zeta}, \Delta t)\end{aligned} \tag{16}$$

where $\boldsymbol{r}$ is the relative degree defined in last subsection, $\Delta\boldsymbol{x} = \boldsymbol{x} - \boldsymbol{x}_0$ is the incremental state and $\Delta\boldsymbol{u} = \boldsymbol{u} - \boldsymbol{u}_0$ is the incremental control. The residual term $\delta(\boldsymbol{\zeta}, \Delta t)$ would be sufficient small if the system's sampling interval is small enough, and $\boldsymbol{\nu}_0$ is obtained from state measurement or system estimation. Meanwhile the incremental control is defined as $\Delta\boldsymbol{u} = \mathcal{B}\left(\boldsymbol{x}_0\right)^{-1}\left(\boldsymbol{\nu} - \boldsymbol{\nu}_0\right)$.

Substituting this $\Delta\boldsymbol{u}$ into (16), the closed loop system in (13) can be transformed into the following format, where $\boldsymbol{A}$, $\boldsymbol{B}$ are the Brunovsky canonical forms.

$$\begin{aligned}\dot{\boldsymbol{\eta}} &= \boldsymbol{f}_0(\boldsymbol{\eta}, \boldsymbol{\xi}) \\ \dot{\boldsymbol{\xi}} &= \boldsymbol{A}\boldsymbol{\xi} + \boldsymbol{B}[\boldsymbol{\nu} + \boldsymbol{\delta}(\boldsymbol{\zeta}, \Delta t)]\end{aligned} \tag{17}$$

$$\boldsymbol{\zeta} = [\boldsymbol{\eta}; \boldsymbol{\xi}] \tag{18}$$

Furthermore, using the following Lemma, stabilty of the whole system will be analyzed in next section.

Lemma 4.1 (Khalil (2014), Lemma 13.4). If $\|\boldsymbol{\delta}(\boldsymbol{\zeta}, \Delta t)\| \leq \varepsilon$ for all $\boldsymbol{\zeta}$ and the internal dynamics $\dot{\boldsymbol{\eta}} = \boldsymbol{f}_0(\boldsymbol{\eta}, \boldsymbol{\xi})$ is ISS, then the state $\boldsymbol{\zeta}$ is globally ultimately bounded by some class $\mathcal{K}$ function of ε.

4.3 Fully-Actuated Multirotor Example

In this subsection a thorough model of the designed FAM is deduced and the unmodelled aerodynamics terms in section 3 are treated as model uncertainties in the following stabilty analysis. First, some phisical parameters are introduced as follow

$$\begin{aligned} n_1 &= \frac{l}{I_{xx}} \qquad n_2 = \frac{l}{I_{yy}} \qquad n_3 = \frac{1}{I_{zz}} \\ w_1 &= \frac{I_{yy} - I_{zz}}{I_{xx}} \qquad w_2 = \frac{I_{zz} - I_{xx}}{I_{yy}} \qquad w_3 = \frac{I_{xx} - I_{yy}}{I_{zz}} \end{aligned} \tag{19}$$

where I_{xx}, I_{yy}, I_{zz} is the inertia tensor and l is half length of the drone's fuselage. Moreover the static tilt angle of each actuator defined in section 3.(11) is listed in the following table.

Tilt Angles						
Axis	+X	−X	+Y	−Y	+Z	−Z
Angle α	0	0	$\pi/2$	$-\pi/2$	0	0
Angle β	0	0	0	0	$\pi/2$	$-\pi/2$
Angle γ	$\pi/2$	$-\pi/2$	0	0	0	0

TABLE I. Static tilt angles of the six actuators.

We select quaternion, angular velocity in $\mathscr{F}_B$, position and velocity in $\mathscr{F}_W$ as the state variable, $\boldsymbol{x} = \left[\tilde{\boldsymbol{q}}^T, \boldsymbol{\Omega}^T, \boldsymbol{p}^T, \boldsymbol{v}^T\right]^T$ and $\boldsymbol{h}(\boldsymbol{x}) = \left[\tilde{\boldsymbol{q}}_{1-3}^T, \boldsymbol{p}^T\right]^T$ as the output vector. Then the specific form in (13) is in the following format, $f(\boldsymbol{x})_F = [\, v_x \;\; v_y \;\; v_z \;\; 0 \;\; 0 \;\; g \,]^T$ and

$$f(\boldsymbol{x})_\tau = \begin{bmatrix} -\left(\Omega_x\, q_1 + \Omega_y\, q_2 + \Omega_z\, q_3\right)/2 \\ \left(\Omega_x\, q_0 - \Omega_y\, q_3 + \Omega_z\, q_2\right)/2 \\ \left(\Omega_x\, q_3 + \Omega_y\, q_0 - \Omega_z\, q_1\right)/2 \\ \left(\Omega_x\, q_1 - \Omega_y\, q_2 + \Omega_z\, q_0\right)/2 \\ \Omega_y\, \Omega_z\, w_1 \\ \Omega_x\, \Omega_z\, w_2 \\ \Omega_x\, \Omega_y\, w_3 \end{bmatrix}$$

$$g(\boldsymbol{x})_\tau = \begin{bmatrix} \multicolumn{6}{c}{\mathbf{0}_{4\times 6}} \\ -n_1 & 0 & 0 & n_1 & 0 & 0 \\ 0 & 0 & -n_2 & 0 & 0 & n_2 \\ 0 & -n_3 & 0 & 0 & n_3 & 0 \end{bmatrix} \boldsymbol{f_B}$$

$$g(\boldsymbol{x})_F = \begin{bmatrix} \mathbf{0}_{3\times 3} & \mathbf{0}_{3\times 3} \\ \mathbf{0}_{3\times 3} & \boldsymbol{R}(\tilde{\boldsymbol{q}}) \end{bmatrix} \begin{bmatrix} \multicolumn{6}{c}{\mathbf{0}_{3\times 6}} \\ 0 & -1 & 0 & 0 & -1 & 0 \\ -1 & 0 & 0 & -1 & 0 & 0 \\ 0 & 0 & -1 & 0 & 0 & -1 \end{bmatrix} \boldsymbol{f_B}$$

where $\boldsymbol{f_B} = [f_1, \cdots, f_6]$ is the input force defined in body coordinate (9) and n_i is defined in (19). Furthermore, $f(\boldsymbol{x}) = \left[f(\boldsymbol{x})_\tau^T \quad f(\boldsymbol{x})_F^T\right]^T$, $g(\boldsymbol{x})\boldsymbol{u} = \left[g(\boldsymbol{x})_\tau^T \quad g(\boldsymbol{x})_F^T\right]^T$ and $\mathcal{B}_0(\mathbf{x}) = 2\mathcal{B}(\mathbf{x})$ in (15) is in the following form:

$$\mathcal{B}_0(\mathbf{x}) = \begin{bmatrix} -n_1\, q_0 & n_3\, q_2 & n_2\, q_3 & n_1\, q_0 & -n_3\, q_2 & -n_2\, q_3 \\ -n_1\, q_3 & -n_3\, q_1 & -n_2\, q_0 & n_1\, q_3 & n_3\, q_1 & n_2\, q_0 \\ n_1\, q_2 & n_3\, q_0 & -n_2\, q_1 & -n_1\, q_2 & -n_3\, q_0 & n_2\, q_1 \\ 2\varphi_7 & 2\varphi_3 & 2\varphi_5 & 2\varphi_7 & 2\varphi_3 & 2\varphi_5 \\ 2\varphi_2 & 2\varphi_4 & 2\varphi_9 & 2\varphi_2 & 2\varphi_4 & 2\varphi_9 \\ 2\varphi_6 & 2\varphi_8 & 2\varphi_1 & 2\varphi_6 & 2\varphi_8 & 2\varphi_1 \end{bmatrix} \tag{20}$$

and φ_i in $\mathcal{B}_0(\mathbf{x})$ are shown in Appendix A. After calculation, it's shown that $\det(\mathcal{B}(\mathbf{x})) = \frac{1}{8m^3} n_1 n_2 n_3 q_0$, which is positive when $q_0 \neq 0$ (since $0 \leq q_0 \leq 1$). Hence, it means $\mathcal{B}(\mathbf{x})$ is nonsingular when the FAM's rotation angle about one arbitrary 3D axis is smaller than 180°.

It's not difficult to see that the relative degree of one motion axis such as positon $\boldsymbol{p}_x$ equals 2 while whole degrees of the rigid body $r_0 = \sum_{i=1}^{6} r_i = 2 \times 6 = 12$, which is obviously smaller than the total number of state $\boldsymbol{x}$ that equals 13. Hence, there exists an internal dynamics.

We select $\eta = q_0$ as the internal variable thus according to (Khalil (2014)), when $\xi = 0$, if the zero dynamics $\dot{\eta} = f_0(\eta, 0)$ is asymptotically stable in the domain $D_0 \subset D$, then the whole system is a minimum phase.

After trivially calculation, the system state is a diffeomorphism because of the fact $\frac{\partial \eta}{\partial \boldsymbol{x}}\, \mathrm{g}(\boldsymbol{x}) = \mathbf{0}$ and $\mathcal{B}(\mathbf{x}, \mathbf{t})$ is nonsingular when $q_0 \neq 0$.

Moreover using the quaternion dynamics, i.e., $\|\mathbf{q}\|_2 = \sqrt{\sum_{i=0}^{3} q_i^2} = 1$, it's easy to see that $\dot{\boldsymbol{\eta}} = \boldsymbol{f}_0(\boldsymbol{\eta}, \boldsymbol{\xi})$ is ISS with respect to $\boldsymbol{\xi} = \tilde{\boldsymbol{q}}_{1-3}$.

5. SELF-TRIGGERED CONTROLLER

In this section the self-triggered control is introduced to relieve the communication burden and remove the neccesity of continuous background sensor supervision. Desired performance of the system is also analyzed, which renders the system (13) uniformly globally exponentially stable. Furthermore, to make the self-triggered controller

meaningful, exclusion of Zeno phenomenon (see Li et al. (2020)) is of importance which means the inter-execution time internal should be lower bounded. Finally, the corresponding stabilty of the system (13) is analyzed including the internal dynamics.

5.1 Self-Triggered Policy Analysis

Firstly we consider the linear canonical form defined in (17), a state feedback control is adopted as $\boldsymbol{\nu} = \boldsymbol{K}\boldsymbol{\xi}(t_k)$ where the gain matrix $\boldsymbol{K}$ makes $(\boldsymbol{A}+\boldsymbol{B}\boldsymbol{K})$ Hurwitz and respectively the decaying rate λ is fulfilled for arbitrary sampling interval τ_k where k $\in \mathbb{N}+$.

$$V(\boldsymbol{\xi}(t_{k+1})) \leq V(\boldsymbol{\xi}(t_k))\, e^{-\lambda\tau_k} \tag{21}$$

Since all the control input is deployed on digital platforms, we can define the following sample error during a triggered interval as $\boldsymbol{e}(t) = \boldsymbol{\xi}(t_k) - \boldsymbol{\xi}(t), \quad t \in [t_k, t_{k+1}]$.

Substituting $\boldsymbol{e}(t)$ into (17) renders the following dynamics

$$\begin{bmatrix} \dot{\boldsymbol{\xi}} \\ \dot{\boldsymbol{e}} \end{bmatrix} = \begin{bmatrix} \boldsymbol{A}+\boldsymbol{B}\boldsymbol{K} & \boldsymbol{B}\boldsymbol{K} \\ -\boldsymbol{A}-\boldsymbol{B}\boldsymbol{K} & -\boldsymbol{B}\boldsymbol{K} \end{bmatrix} \begin{bmatrix} \boldsymbol{\xi} \\ \boldsymbol{e} \end{bmatrix} = \boldsymbol{H}_a \boldsymbol{z}_a \tag{22}$$

Then state variable $\boldsymbol{\xi}$ at $t = t_k + m\Delta T_s$, $(m \in \mathbb{N}+)$ can be iterated by the following equation where ΔT_s is the sampling interval and the selection matrix $\boldsymbol{S} = [\mathbf{I}_{n\times n} \quad \mathbf{0}_{n\times n}]$, where n is the number of the state $\boldsymbol{\xi}$.

$$\begin{aligned} \boldsymbol{M_a} &= e^{\boldsymbol{H}_a \Delta T_s} \\ \boldsymbol{\xi}(t_k + m\Delta T_s) &= \boldsymbol{S}\boldsymbol{M_a}^m \boldsymbol{z}_a(t_k) \end{aligned} \tag{23}$$

Select $V(\boldsymbol{\xi}) = \boldsymbol{\xi}^T\boldsymbol{P}\boldsymbol{\xi}$ as the Lyapunov function and $(\boldsymbol{A}+\boldsymbol{B}\boldsymbol{K})^T\boldsymbol{P} + \boldsymbol{P}(\boldsymbol{A}+\boldsymbol{B}\boldsymbol{K}) = -\boldsymbol{I}$ is satisfied, then $\dot{V}(\boldsymbol{\xi}) = -2\boldsymbol{\xi}^T\boldsymbol{\xi}$ is negative. Utilizing the matrix vec operator (see Graham (1981)), thus its prediction form is defined as

$$\begin{aligned} &V_a(\boldsymbol{\xi}(t_k + m\Delta T_s)) = \boldsymbol{\xi}^T(t_k + m\Delta T_s)\,\boldsymbol{P}\boldsymbol{\xi}(t_k + m\Delta T_s) \\ &= \mathrm{vec}(\boldsymbol{P})^T(\boldsymbol{\xi}(t_k + m\Delta T_s) \otimes \boldsymbol{\xi}(t_k + m\Delta T_s)) \\ &= \mathrm{vec}(\boldsymbol{P})^T(\boldsymbol{S}\otimes\boldsymbol{S})(\boldsymbol{M_a}\otimes\boldsymbol{M_a})^m \boldsymbol{Z}_a \end{aligned} \tag{24}$$

where $\boldsymbol{Z}_a$ is defined as $(\boldsymbol{z}_a(t_k) \otimes \boldsymbol{z}_a(t_k))$.

Similarly another augmented linear system is designed to satisfy the expected dynamic performance such as decaying rate or convergence time, et al.

$$\begin{bmatrix} \dot{\boldsymbol{\xi}}_b \\ \mathbf{0} \end{bmatrix} = \begin{bmatrix} \boldsymbol{A}+\boldsymbol{B}\boldsymbol{K} & \mathbf{0}_{n\times n} \\ \mathbf{0}_{n\times n} & \mathbf{0}_{n\times n} \end{bmatrix} \begin{bmatrix} \boldsymbol{\xi}_b \\ \mathbf{0} \end{bmatrix} = \boldsymbol{H}_b \boldsymbol{z}_b \tag{25}$$

For the simplicity and efficiency of digital implementation, we denote some intermediate variables which can be calculated off-line as

$$\begin{aligned} \boldsymbol{F} &= \mathrm{vec}(\boldsymbol{P})^T(\boldsymbol{S}\otimes\boldsymbol{S}) \\ \boldsymbol{G}_a &= (\boldsymbol{M_a}\otimes\boldsymbol{M_a})^m \\ \boldsymbol{G}_b &= (\boldsymbol{M_b}\otimes\boldsymbol{M_b})^m \end{aligned} \tag{26}$$

Finally the direct consequence for satisfying the desired performance as (25) is transformed into the next inequality $V_a(\boldsymbol{\xi}(t_k + m\Delta T_s)) \leq V_b(\boldsymbol{\xi}_b(t_k + m\Delta T_s))$, i.e., $\boldsymbol{F}(\boldsymbol{G_a}\boldsymbol{Z}_a - \boldsymbol{G_b}\boldsymbol{Z}_b) \leq 0$ and we describe the self-triggered interval as a set for the convinence of analysis.

$$\begin{aligned} m_k &= \max\{i \mid \sigma(\boldsymbol{\xi}(t_k), i\Delta T_s) \leq 0\} \\ \sigma(\boldsymbol{\xi}(t_k), i\Delta T_s) &= \boldsymbol{F}(\boldsymbol{G_a}\boldsymbol{Z}_a - \boldsymbol{G_b}\boldsymbol{Z}_b), \forall i \in [0, M_{max}] \end{aligned} \tag{27}$$

where M_{max} is the maximum discrete sampling number that system is allowed to work in an open-loop mode. Notice that in (16), smaller model mismatch $\delta(\boldsymbol{\zeta}, \Delta t)$ requires samller sampling time interval. Therefore, choice of the M_{max} would be a compromise between system robustness and communication loads.

Lemma 5.1 (Mazo and Tabuada (2009)). Closed loop system $\dot{\boldsymbol{\xi}} = \boldsymbol{A}\boldsymbol{\xi} + \boldsymbol{B}[\boldsymbol{K}\boldsymbol{\xi} + \boldsymbol{\delta}]$ is exponentially uniformly ISS under the self-triggered control policy as (27).

$$\begin{aligned} \|\boldsymbol{\xi}(t)\| &\leq g(\Delta T_s, M_{\max})\,\rho_P \|\boldsymbol{\xi}(t_0)\| e^{-\lambda t} \\ &+ \gamma_P(\|\delta\|_\infty)\,\frac{\lambda_m^{-\frac{1}{2}}(P)\, g(\Delta T_s, M_{\max})}{1 - e^{-\lambda t_{\min}}} + \gamma_I(\|\delta\|_\infty) \end{aligned} \tag{28}$$

where $\rho_P = (\lambda_M(\boldsymbol{P})/\lambda_m(\boldsymbol{P}))^{\frac{1}{2}}$, λ is defined in (21), and the left intermediate functions $g(\Delta T_s, M_{\max})$, $\gamma_I(x)$ and $\gamma_P(x)$ can be found in equation (15) in the reference paper.

5.2 Zeno Phenomenon Avoidance

In order to make the self-triggered controller meaningful, Zeno behaviour should be excluded otherwise infinite control sequences will happen which means $\inf_{k\in\mathbb{N}+}\{t_{k+1} - t_k\}$ should be some strict positive value and $\lim_{k\to\infty} t_k = \infty$.

Lemma 5.2 (Bahavarnia (2021)). The inter-execution time under policy (27) is lower bounded by $\tau^*_{\min}$ which is defined as:

$$\begin{aligned} \tau^*_{\min} &= \min\left\{\tau \in \mathbb{R}^+ : \det(\boldsymbol{M}(\tau)) = 0\right\} \\ \boldsymbol{M}(\tau) &= \boldsymbol{S}\left(\mathrm{e}^{\boldsymbol{H}_a^T\tau}\boldsymbol{S}^T\boldsymbol{P}\boldsymbol{S}\mathrm{e}^{\boldsymbol{H}_a\tau} - \boldsymbol{S}^T\boldsymbol{P}\boldsymbol{S}\mathrm{e}^{-2\lambda\tau}\right)\boldsymbol{S}^T \end{aligned} \tag{29}$$

Recall the triggered sequences defined in (27), sampling interval $\tau_k \in [\tau^*_{\min}, M_{max}\Delta T_s]$ and no Zeno phenomenon would happen.

5.3 Input-to-state Stabilty Analysis

Lemma 5.3: Closed loop system for the designed FAM defined in (17) is globally ultimately bounded by a class $\mathcal{K}$ function about $\|\boldsymbol{\delta}(\boldsymbol{\zeta}, \Delta t)\|_\infty$ under the self-triggered control policy as (27).

Proof. Select $V(\boldsymbol{\xi}) = \boldsymbol{\xi}^T\boldsymbol{P}\boldsymbol{\xi}$ as the Lyapunov function (see analysis under (23)) and use $\|\boldsymbol{\delta}\|_\infty$ to represent the infinity norm of $\boldsymbol{\delta}(\boldsymbol{\zeta}, \Delta t)$, according to Theorem 4.19 in Khalil (2014) and the Rayleigh-Ritz inequality in Rugh (1996), several properties are satisfied as $\alpha_1(\|\boldsymbol{\xi}\|_2) \leq V(\boldsymbol{\xi}) \leq \alpha_2(\|\boldsymbol{\xi}\|_2), \alpha_1(\|\boldsymbol{\xi}\|_2) \triangleq \lambda_{\mathrm{m}}(\boldsymbol{P})\|\boldsymbol{\xi}\|_2^2$ and $\alpha_2(\|\boldsymbol{\xi}\|_2) \triangleq \lambda_M(\boldsymbol{P})\|\boldsymbol{\xi}\|_2^2$.

According to Lemma 5.1, $\boldsymbol{\xi}(t)$ is exponentially uniformly ISS and $\|\boldsymbol{\xi}(t)\|_2 \leq \beta(\|\boldsymbol{\xi}(t_0)\|_2, t - t_0) + \gamma(\|\boldsymbol{\delta}\|_\infty)$ where functions $\beta(x,t)$ and $\gamma(x)$ are defined as below

$$\beta(x,t) = \rho_P g(\Delta, N_{\max})\, e^{-\lambda t} x \tag{30}$$

$$\gamma(x) = \gamma_I(x)\left(\frac{\rho_P^2 g(\Delta, N_{\max})}{1 - e^{-\lambda t_{\min}}} + 1\right) \tag{31}$$

Moreover the property of $\mathcal{KL}$ function $\beta(x,t)$ guarantees the following inequality satisfied in a finite time Δ_{T_1}

$$\begin{aligned} &\|\boldsymbol{\xi}(t)\|_2 \leq \beta(\|\boldsymbol{\xi}(t_0)\|_2, t - t_0), t_0 \leq \forall t \leq t_0 + \Delta_{T_1} \\ &\|\boldsymbol{\xi}(t)\|_2 \leq \alpha_1^{-1}(\alpha_2(\gamma(\|\boldsymbol{\delta}\|_\infty))), \forall t \geq t_0 + \Delta_{T_1} = t_1 \\ &\bar{\varrho} \triangleq \alpha_1^{-1}(\alpha_2(\gamma(\|\boldsymbol{\delta}\|_\infty))) = \rho_P\gamma(\|\boldsymbol{\delta}\|_\infty) \end{aligned} \tag{32}$$

Remember in Lemma 4.1, an ISS internal dynamics $\dot{\boldsymbol{\eta}} = \boldsymbol{f}_0(\boldsymbol{\eta}, \boldsymbol{\xi})$ leads to whole system ultimately bounded by a class $\mathcal{K}$ function. Then the specific $\mathcal{K}$ function form is deduced. According to the ISS properties, the internal dynamics can be bounded by $\|\boldsymbol{\eta}(t)\|_2 \leq \beta_0\left(\|\boldsymbol{\eta}\left(t_0\right)\|_2, t - t_0\right) + \gamma_0\left(\bar{\varrho}\right)$ for some function $\gamma_0 \in$ class $\mathcal{K}$.

And $\boldsymbol{\eta}(t)$ is finally bounded by $\varepsilon\bar{\varrho}$ at time instant t_1 for some small positive value ε. Finally we can prove that the designed FAM system (17) under self-triggered control policy (27) is globally ultimately bounded.

$$\|\boldsymbol{\zeta}(t)\|_2 \leq \|\boldsymbol{\xi}(t)\|_2 + \|\boldsymbol{\eta}(t)\|_2 \leq (\varepsilon + 1)\,\bar{\varrho} + \gamma_0\left(\bar{\varrho}\right), \forall t \geq t_1$$

6. SIMULATION RESULTS

In this section some simulation results are illustrated to verify the effictiveness of the proposed self-triggered controller. We consider the novel FAM which has been exhaustively described in Section 4 and give a six-dimensional fully decoupled spatial trajectory as the tracking mission

$$\begin{aligned} x_d\left(t\right) &= 1.2\sin(2t + \pi/2) \\ y_d\left(t\right) &= 1.2\sin(2t + \pi/2) \\ z_d\left(t\right) &= 0.4t - 1 \end{aligned}$$

The translational motion is a 3D helix curve in $\mathscr{F}_W$, meanwhile attitude motion is set as

$$\begin{aligned} \boldsymbol{q_d} &= \cos\left(\theta_d(t)/2\right) + \boldsymbol{n}_d \sin\left(\theta_d(t)/2\right) \\ \theta_d(t) &= 1\sin(3t),\ \boldsymbol{n}_d = [1, 3, -1]^T \end{aligned}$$

To show the robustness of the proposed controller, an intuitively internal time-varying model uncertainty and external disturbances $\boldsymbol{d}_i(t) = 0.08\sin(10t)$ (directly added on each channel of (13)) is imposed to the FAM. Notice that the nominal model is $m_n = 6$, $\boldsymbol{I}_{tn} = diag[3, 3, 3.1]$ and all the units are in $\boldsymbol{SI}$.

$$\begin{aligned} m(t) &= 5 + 2\sin\left((9/4)\,t\right) \\ \boldsymbol{I}_{\mathrm{t}}(t) &= diag[2, 5, 7] \end{aligned} \tag{33}$$

Gain of the state feedback control $v = K\xi$ is chosen as $[-6.3, -5]$, off-line arranged feedforward input frequency M_{max} (see (27)) is set by 50 Hz and system sampling interval ΔT_s is set by 2ms.

The translational trajectory tracking results are depicted in Fig. 3 and all the perturbations are added at instant $t = 6s$ corresponding to the red zone. Although intense perturbations as (33) is imposed on the FAM, the translational motion still shows great robustness under self-triggered controller (27). Moreover the acceleration curve is also depicted in Fig. 4 which demonstrate the self-triggered policy more intuitively. Attitude trajectories are illustrated in Fig. 5 which still possess robustness to perturbations simultaneously. Finally we give the self-triggered time stamp with the error Lyapunov function $V_a\left(\boldsymbol{e}(t)\right)$ (see (24)) and the designed one $V_b\left(\boldsymbol{e}(t)\right)$ in Fig. 6, from which we can conclude that the actual Lyapunov function $V_a\left(\boldsymbol{e}(t)\right)$ is always smaller than $V_b\left(\boldsymbol{e}(t)\right)$, otherwise an event is triggered to make sure the designed policy remains valid. $V_0\left(\boldsymbol{e}(t)\right)$ (see (21)) is a reference candidate that keeps decaying with static rate λ since the initial time.

7. CONCLUSION

In this paper, we proposed a robust self-triggered control policy for feedback linearizable nonlinear systems. This algorithm is applied on a novel fully actuated multirotor and arbitrary 6-dimensional fully decoupled motion can be accomplished. To cope with the ubiquitous uncertainties and disturbances, an incremental discrete time controller is adopted instead of the traditional precise nonlinear compensation method. Communication burden is relieved and continuous background sensor monitoring is no more needed. Rigorous stabilty analysis for both internal and external dynamics under perturbations is proved, meanwhile detailed simulation results are shown to verify the validity of the proposed policies.

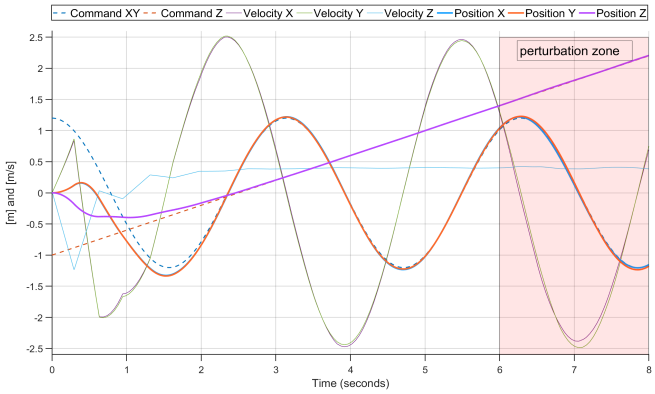

Fig. 3. Position and velocity tracking trajectories.

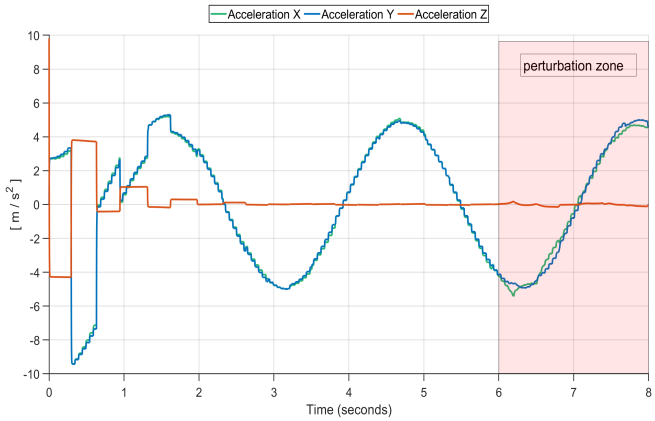

Fig. 4. Acceleration tracking trajectories.

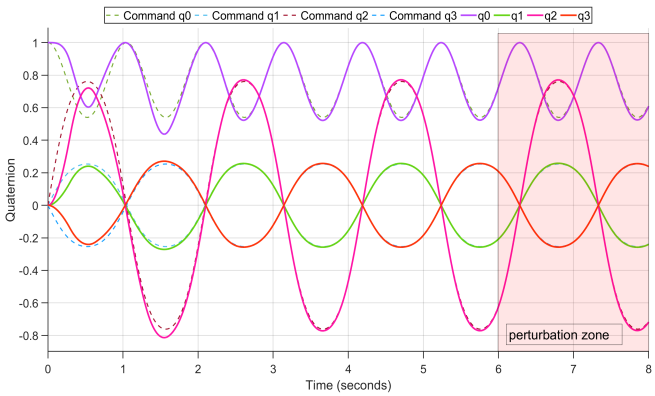

Fig. 5. Attitude tracking trajectories.

Appendix A. COLLECTION OF SYMBOLS

Here, φ_i in $\mathcal{B}_0(\mathbf{x})$ in (20) are listed as below.

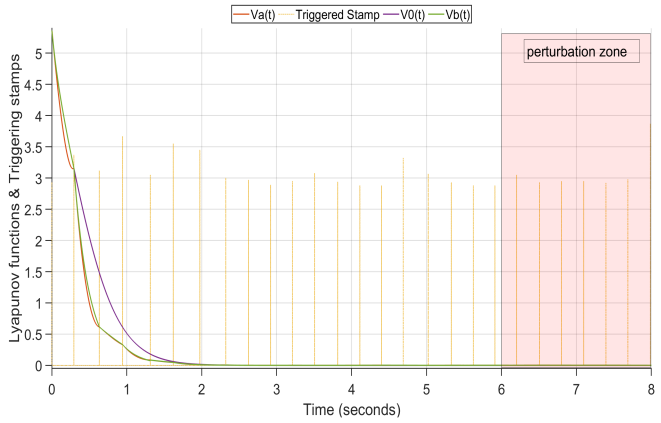

Fig. 6. Self-triggered stamps with Lyapunov function, notice that the triggered time intervals are in units of 100 ms.

$$
\begin{aligned}
\varphi_1 &= -\left({q_0}^2 - {q_1}^2 - {q_2}^2 + {q_3}^2\right)/m \\
\varphi_2 &= -\left({q_0}^2 - {q_1}^2 + {q_2}^2 - {q_3}^2\right)/m \\
\varphi_3 &= -\left({q_0}^2 + {q_1}^2 - {q_2}^2 - {q_3}^2\right)/m \\
\varphi_4 &= -\left(2\,q_0\,q_3 + 2\,q_1\,q_2\right)/m \\
\varphi_5 &= -\left(2\,q_0\,q_2 + 2\,q_1\,q_3\right)/m \\
\varphi_6 &= -\left(2\,q_0\,q_1 + 2\,q_2\,q_3\right)/m \\
\varphi_7 &= \left(2\,q_0\,q_3 - 2\,q_1\,q_2\right)/m \\
\varphi_8 &= \left(2\,q_0\,q_2 - 2\,q_1\,q_3\right)/m \\
\varphi_9 &= \left(2\,q_0\,q_1 - 2\,q_2\,q_3\right)/m
\end{aligned}
$$

REFERENCES

Abdelrahim, M., Postoyan, R., Daafouz, J., and Nešić, D. (2016). Stabilization of Nonlinear Systems Using Event-Triggered Output Feedback Controllers. *IEEE Transactions on Automatic Control*, 61(9), 2682–2687.

Bahavarnia, M. (2021). Comments on "An ISS self-triggered implementation of linear controllers" [Automatica 46 (2010) 1310–1314]. *Automatica*, 133, 109755.

Barfoot, T.D. (2017). *State Estimation for Robotics*. Cambridge University Press, Cambridge.

Chang, D.E. and Eun, Y. (2017). Global Chartwise Feedback Linearization of the Quadcopter With a Thrust Positivity Preserving Dynamic Extension. *IEEE Transactions on Automatic Control*, 62(9), 4747–4752.

Graham, A. (1981). *Kronecker Products and Matrix Calculus: With Applications*. Ellis Horwood Series in Mathematics and Its Applications. Horwood ; Halsted Press, Chichester : New York.

Huang, Y., Pool, D., Stroosma, O., and Chu, Q. (2017). Incremental Nonlinear Dynamic Inversion Control for Hydraulic Hexapod Flight Simulator Motion Systems * *The first author is sponsored by Chinese Scholarship Council. *IFAC-PapersOnLine*, 50(1), 4294–4299.

Kai, J.M., Allibert, G., Hua, M.D., and Hamel, T. (2017). Nonlinear feedback control of Quadrotors exploiting First-Order Drag Effects. *IFAC-PapersOnLine*, 50(1), 8189–8195.

Kaufman, E., Caldwell, K., Lee, D., and Lee, T. (2014). Design and development of a free-floating hexrotor UAV for 6-DOF maneuvers. In *2014 IEEE Aerospace Conference*, 1–10. IEEE, Big Sky, MT, USA.

Khalil, H.K. (2014). *Nonlinear Systems*. Always Learning. Pearson Education, Harlow, pearson new internat. ed., 3. ed edition.

Lee, T., Leok, M., and McClamroch, N.H. (2010). Geometric tracking control of a quadrotor UAV on SE(3). In *49th IEEE Conference on Decision and Control (CDC)*, 5420–5425. IEEE, Atlanta, GA.

Li, C., Zhang, Y., and Li, P. (2017). Full control of a quadrotor using parameter-scheduled backstepping method: Implementation and experimental tests. *Nonlinear Dynamics*, 89(2), 1259–1278.

Li, X., Peng, D., and Cao, J. (2020). Lyapunov Stability for Impulsive Systems via Event-Triggered Impulsive Control. *IEEE Transactions on Automatic Control*, 65(11), 4908–4913.

Liu, T. and Jiang, Z.P. (2019). Event-Triggered Control of Nonlinear Systems With State Quantization. *IEEE Transactions on Automatic Control*, 64(2), 797–803.

Mayhew, C.G., Sanfelice, R.G., and Teel, A.R. (2011). Quaternion-Based Hybrid Control for Robust Global Attitude Tracking. *IEEE Transactions on Automatic Control*, 56(11), 2555–2566.

Mazo, M. and Tabuada, P. (2009). Input-to-state stability of self-triggered control systems. In *Proceedings of the 48h IEEE Conference on Decision and Control (CDC) Held Jointly with 2009 28th Chinese Control Conference*, 928–933.

Mellinger, D. and Kumar, V. (2011). Minimum snap trajectory generation and control for quadrotors. In *2011 IEEE International Conference on Robotics and Automation*, 2520–2525.

Michieletto, G., Cenedese, A., Zaccarian, L., and Franchi, A. (2017). Nonlinear Control of Multi-Rotor Aerial Vehicles Based on the Zero-Moment Direction. *IFAC-PapersOnLine*, 50(1), 13144–13149.

Rugh, W.J. (1996). *Linear System Theory*. Prentice Hall Information and System Sciences Series. Prentice Hall, Upper Saddle River, N.J, 2nd ed edition.

Siciliano, B. and Khatib, O. (eds.) (2016). *Springer Handbook of Robotics*. Springer International Publishing, Cham.

Sontag, E. (1989). Smooth stabilization implies coprime factorization. *IEEE Transactions on Automatic Control*, 34(4), 435–443.

Staub, N., Bicego, D., Sable, Q., Arellano, V., Mishra, S., and Franchi, A. (2018). Towards a Flying Assistant Paradigm: The OTHex. In *2018 IEEE International Conference on Robotics and Automation (ICRA)*, 6997–7002. IEEE, Brisbane, QLD.

Suarez, A., Heredia, G., and Ollero, A. (2018). Physical-Virtual Impedance Control in Ultralightweight and Compliant Dual-Arm Aerial Manipulators. *IEEE Robotics and Automation Letters*, 3(3), 2553–2560.

Tabuada, P. (2007). Event-Triggered Real-Time Scheduling of Stabilizing Control Tasks. *IEEE Transactions on Automatic Control*, 52(9), 1680–1685.

Tallapragada, P. and Chopra, N. (2013). On Event Triggered Tracking for Nonlinear Systems. *IEEE Transactions on Automatic Control*, 58(9), 2343–2348.

Wang, X. and Lemmon, M.D. (2008). State Based Self-triggered Feedback Control Systems with $\mathscr{L}2$ Stability. *IFAC Proceedings Volumes*, 41(2), 15238–15243.